Crimson Publishers
Wings to the Research

Research Article

Phase-Engineered Ni-MoS_2 Thin Films: Optoelectronic Tuning and Enhanced Photocatalytic Activity

Bahadivand Chegini S[1], Khanlary M[1]* and Baghshahi S[2]

[1]Department of Physics, Imam Khomeini International University, Iran

[2]Department of Materials Science and Engineering, Imam Khomeini International University, Iran

ISSN: 2576-8840

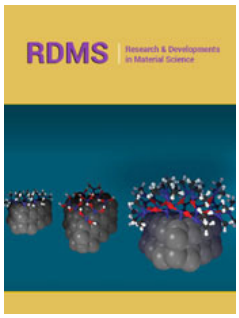

***Corresponding author:** Khanlary M, Department of Physics, Imam Khomeini International University, Iran

Submission: June 30, 2026
Published: August 10, 2026

Volume 23 - Issue 1

How to cite this article: Bahadivand Chegini S, Khanlary M* and Baghshahi S. Phase-Engineered Ni-MoS_2 Thin Films: Optoelectronic Tuning and Enhanced Photocatalytic Activity. Res Dev Material Sci. 23(1). RDMS. 001055. 2026.
DOI: 10.31031/RDMS.2026.23.001055

Abstract

The inherent metastability of the 1T phase of MoS_2 presents a significant synthetic challenge. However, our approach utilizing spray pyrolysis has demonstrated a novel pathway for its stabilization. The strategic introduction of oxygen during this process is crucial; it mediates interfacial interactions that substantially lower the material's surface energy, thereby effectively inhibiting the thermodynamically favored 1T→2H phase transition and preserving the metastable 1T structure for potential applications. In this work Ni-doped MoS_2 thin films with nickel concentrations ranging from 0 to 7 at. % were synthesized via spray pyrolysis. Structural, optical, and chemical characterizations were conducted using XRD, Raman spectroscopy, UV-Vis spectroscopy, PL, FTIR, and AFM. XRD and Raman results verified the coexistence of semiconducting 2H and metallic 1T phases. UV-Vis analysis showed a reduction in the optical band gap from 1.84eV to 1.59eV with increasing Ni content, which is attributed to the formation of impurity-induced energy levels within the band structure. FTIR measurements indicated decreased surface hydrophilicity upon Ni incorporation, while AFM images revealed an increase in surface roughness. Photocatalytic degradation of methylene blue under visible-light irradiation improved markedly from 53% for pristine MoS_2 to 99.4% for the 7 at. % Ni-doped film, due to the higher density of active edge sites and defect-induced charge trapping. In general, these findings demonstrate that Ni doping is a highly effective approach for tuning the optoelectronic properties of MoS_2 and substantially enhancing its photocatalytic performance.

Introduction

Two-dimensional Transition Metal Dichalcogenides (TMDs), particularly molybdenum disulfide (MoS_2), have attracted extensive research interest due to their exceptional layer-dependent physicochemical properties. MoS_2 exhibits intrinsic n-type conductivity arising from native nonmetallic defects and possesses a tunable electronic band gap, ranging from 1.2eV (indirect) in the bulk to 1.9eV (direct) in the monolayer regime [1,2]. The emergence of a direct band gap in few-layer configurations makes MoS_2 an appealing material for advanced optoelectronic applications, including UV-visible and near-infrared photodetectors. However, conventional synthesis methods such as mechanical exfoliation and Chemical Vapor Deposition (CVD), despite producing high-quality crystals, remain limited by scalability, cost, and process complexity, constraining their suitability for large-scale industrial implementation [3].

The 1T phase of MoS_2, notwithstanding its distinctive electronic properties, has historically been hampered in practical applications by its inherent metastability, frequently yielding to the more stable 2H phase during post-synthesis processing. Conventional methodologies have encountered significant challenges in circumventing this phase transformation. Our findings demonstrate that the spray pyrolysis technique, by virtue of its intrinsic characteristics and the presence of oxygen, effectively sustains the metallic 1T phase, thereby inhibiting the transition to the semiconducting 2H phase. This breakthrough not only establishes a reliable synthetic route for phase-pure 1T -MoS_2 but also unlocks avenues for the exploitation of its exotic properties in advanced electronic and catalytic devices, addressing a critical bottleneck within the field. Spray pyrolysis has emerged as a simple, cost-effective, and scalable alternative for depositing MoS_2 thin films under ambient conditions. This technique offers precise control over precursor chemistry and enables homogeneous incorporation of dopant

species into the MoS_2 lattice, making it particularly suitable for the fabrication of intentionally doped semiconductor films over large areas [4]. Doping MoS_2 with transition metals has proven to be an efficient strategy for tailoring its structural, electronic, and chemical properties. Among various dopants, nickel (Ni) has gained attention due to its ability to modify lattice periodicity, modulate the Fermi level, and increase the density of charge carriers [5,6]. Previous studies have shown that Ni doping enhances photocatalytic activity, Hydrogen Evolution Reaction (HER) performance, and the operational characteristics of electronic devices [7-9]. Specifically, incorporation of Ni introduces impurity states within the band structure, leading to band gap narrowing and improved visible-light absorption [10].

Beyond electronic modulation, Ni doping also plays a significant role in the phase behavior of MoS_2. While the semiconducting 2H polymorph is thermodynamically stable under ambient conditions, the metallic 1T and distorted 1T′ phases exhibit markedly higher electrical conductivity and catalytic activity [11]. Mixed-phase structures composed of coherent 2H/1T domains have been experimentally achieved, characterized by atomically sharp phase boundaries and crystallographically matched interfaces that form in-plane metal/semiconductor heterostructures [12]. Such biphasic configurations offer promising opportunities for next-generation optoelectronic devices, including field-effect transistors, photodetectors, and photocatalytic systems [13,14].

Sulfur vacancies (VS), whether intrinsic or introduced during synthesis, play a critical role in governing phase transitions and catalytic behavior. These vacancies increase electron carrier concentration and facilitate the 2H phase to1T phase transformation in TMDs [15,16]. Moreover, edge sites with unsaturated coordination serve as active centers for catalytic reactions, and their density can be substantially increased through controlled doping strategies [17].

Despite notable progress, systematic investigations into the combined effects of Ni doping on phase evolution, band structure engineering, and photocatalytic performance of spray-pyrolyzed MoS_2 thin films remain limited. In particular, the relationship between Ni concentration, stabilization of the metallic 1T phase, and enhancement of visible-light-driven photocatalytic performance requires further elucidation. In this study, we synthesize Ni-doped MoS_2 thin films with varying Ni concentrations (0, 3, 5, and 7 at. %) via spray pyrolysis and examine the influence of Ni incorporation on structural phase evolution, optical band gap modulation, surface morphology, and photocatalytic degradation of methylene blue under visible-light irradiation. Our findings demonstrate that Ni doping simultaneously induces band gap narrowing, stabilizes the metallic 1T phase, and markedly enhances photocatalytic efficiency, achieving a degradation rate of 99.4% for the 7 at. % Ni-doped sample.

Experimental

In this study, molybdenum disulfide (MoS_2) thin films were fabricated via the spray pyrolysis method. Glass substrates with dimensions of 1cm × 2cm were used for film deposition. Prior to deposition, the substrates were ultrasonically cleaned in acetone at 27 °C for 15 minutes, followed by 15 minutes of treatment in methanol under identical conditions. They were then rinsed with deionized water (DW) and dried using a nitrogen (N_2) stream. Finally, the substrates were placed in an oven at 100 °C for 15 minutes to remove residual moisture.

To prepare MoS_2 precursor solution, 0.61g of ammonium heptamolybdate tetrahydrate ($(NH_4)_6Mo_7O_{24}.4H_2O$) and 0.21g of thiourea ($CS(NH_2)_2$), both sourced from Sigma-Aldrich, were separately dissolved in 25mL of DW. The solutions were then combined and stirred magnetically at 1800rpm at room temperature until a clear and colorless precursor solution was obtained. The substrates were placed on a hot plate preheated to 350 °C, and 50mL of the precursor solution was sprayed at a flow rate of 1.5mL/min, with each spray burst lasting 10 seconds. The nozzle-to-substrate distance was maintained at 35cm throughout the process. The Mo/S molar ratio in the precursor was 1:2.1. Ni-doped MoS_2 films were synthesized following the same procedure by adding 3, 5, and 7 wt.% of $NiSO_4 \cdot 6H_2O$ to the composite solution (Table 1). Structural characteristics, chemical composition, and surface morphology of the resulting samples were examined using X-ray Diffraction (XRD) and Atomic Force Microscopy (AFM).

Table 1: Percentage and Composition of the Ni-MoS_2 solution.

Ni Doping (%)	Ammonium Hepta Molybdate (g)	Thiourea (g)	Nickel Sulfate Hexahydrate (g)	Deionized Water (ml)
0	0.61	0.21	-	50
3	0.61	021	0.02561	50
5	0.61	0.21	004320	50
7	0.61	0.21	0.06437	50

The photocatalytic activity of the samples was evaluated via Methylene Blue degradation. For this purpose, A solution was prepared by dissolving 20mg of MB in 18mL of deionized water (DW). The pH was adjusted to 3 by adding 0.1mL of HCl. This mixture was stirred at room temperature for 10 minutes to ensure homogeneity. Subsequently, separate aliquots of this solution were loaded with the photocatalysts (pristine MoS_2 and Ni-doped MoS_2). These suspensions were then stirred at room temperature for 120 minutes under visible light irradiation (80W lamp).

Results and Discussion

Structural analysis

The structural properties of pristine MoS_2 and Ni-doped MoS_2 thin films were examined using X-ray Diffraction (XRD), as shown in Figure 1. The primary diffraction peaks of MoS_2 correspond to the (002) and (100) planes of the hexagonal 2H-MoS_2 phase, appearing at 2θ values of approximately 14.03° and 33°, respectively. An additional peak observed at around 10.40° is attributed to the (002) (sometimes labeled as (001)) reflection of the metastable 1T-MoS_2 phase. The presence of this peak at a lower 2θ angle indicates an expanded interlayer spacing associated with the octahedral coordination of the 1T phase, in contrast to the trigonal prismatic structure characteristic of the 2H phase.

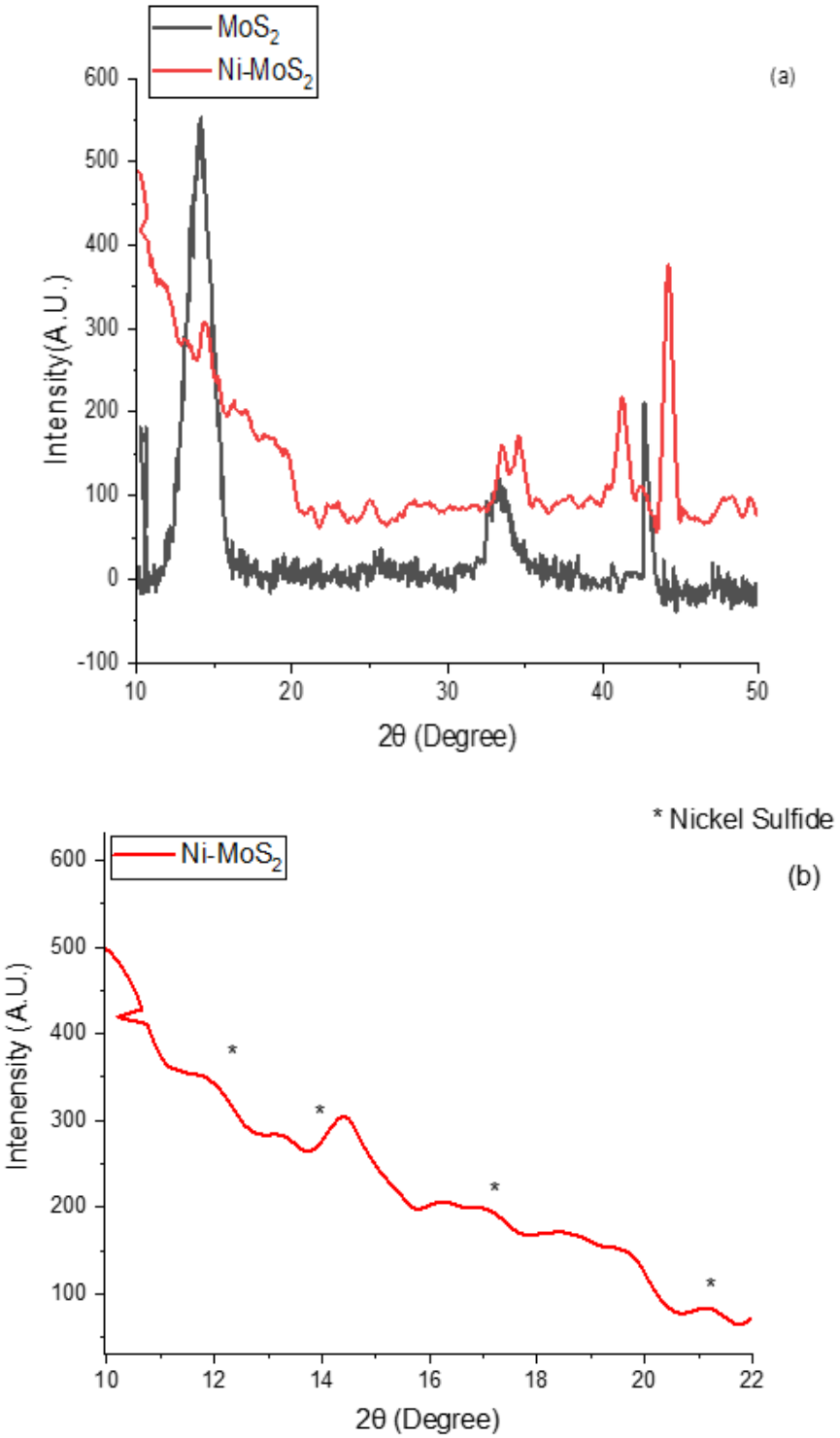

Figure 1: a) XRD patterns of MoS_2 and Ni-MoS_2 films and b) Focus on Ni-induced lattice distortions and secondary phases in the Ni-MoS_2 film within the 10°- 22° 2θ range.

The stabilization of the 1T phase is generally challenging in conventional synthesis routes. In this work, its relative stability is likely facilitated by the non-equilibrium growth kinetics inherent to the spray pyrolysis process, which promote the nucleation and retention of the metastable metallic phase. Moreover, the slight broadening of diffraction peaks and the presence of a weak amorphous background suggest incomplete crystallization, most likely influenced by the substrate temperature during deposition. This parameter could be further optimized to enhance crystalline quality.

Upon Ni incorporation, two additional features appear at approximately 34.4° and 42°, corresponding to nickel-induced

lattice perturbations within the MoS_2 host matrix. A more intense diffraction peak near 44° is attributed can be attributed to metallic nickel. Ni doping also induces a noticeable shift in the (002) diffraction peak toward lower angles, indicating an increase in interlayer spacing (d-spacing). This behavior supports the incorporation of Ni atoms into the MoS_2 lattice and the associated lattice distortion.

Previous studies have reported that the magnetic properties of MoS_2 are strongly dependent on the coexistence of the 1T and 2H phases [18,19] The observed ferromagnetism is often attributed to the intrinsic behavior of mixed-phase 1T/2H MoS_2 systems, whereas the 1T phase alone typically does not exhibit significant room-temperature ferromagnetism. Experimental evidence has also demonstrated that coherent mixed-phase structures with atomically sharp interfaces and lattice matching can form in MoS_2, creating in-plane metal/semiconductor heterostructures that are promising for next-generation optoelectronic and photoelectric devices [20,21].

Sulfur vacancies (Vs) play a critical role in stabilizing the 1T phase and modulating magnetic and electronic behavior. These vacancies increase the electron carrier concentration in the 1T phase and generate localized paramagnetic centers. Additionally, the presence of Vs lowers the energy barrier for the 2H-to-1T phase transition, particularly in two-dimensional materials where quantum confinement enhances phase instability. Nickel is widely recognized as an effective dopant for enhancing the magnetic response of MoS_2, even at low concentrations, and has been reported to improve its performance in gas sensing applications.

Lattice parameter and crystallite size analysis

The lattice parameter (a) for the hexagonal MoS_2 structure was calculated using the standard relation [22]:

$$\frac{1}{d^2}=\frac{4}{3}\left(\frac{h^2+k^2+hk}{a^2}\right)+\frac{l^2}{c^2} \quad (1)$$

where d is the plane distance and h, k and l are the Miller indices of the corresponding diffraction planes.

The crystallite size was estimated using the Scherrer equation [23]:

$$D=\frac{K\lambda}{\beta\cos\theta} \quad (2)$$

where K is the shape factor constant, (0.9), λ is x-ray wavelength (1.5406Å), β is the full width at half maximum (FWHM) and θ is the corresponding Bragg angle.

Based on the calculations, the lattice planes distance decreased from 3.13Å for pristine MoS_2 to 3.00Å for Ni-doped MoS_2 films. The reduction in the interlayer spacing is attributed to the interstitial incorporation of Ni atoms within the MoS_2 lattice, which significantly modulates the local bonding configuration and interlayer interactions. This structural contraction, rather than being solely a consequence of ionic radii mismatch, indicates that Ni incorporation-likely mediated by lattice strain and perturbations in the local electronic density-serves as a primary driver for the observed interlayer spacing. These findings suggest that Ni-doping can be effectively employed to tune the material's physicochemical and catalytic performance.

Also, the calculations indicate that Ni incorporation increased the crystallite size from 4.65nm in undoped MoS_2 to approximately 18nm for the Ni-doped films. This enhancement in crystallite size may result from Ni-induced atomic agglomeration and the facilitation of grain coalescence during film growth.

In addition, Figure 1(b) exhibits weak but distinguishable reflections in the 2θ range of 11-21°. These low-intensity features are attributed to the presence of a minor secondary phase, identified as nickel sulfide (NiS). This assignment is consistent with previously reported diffraction data corresponding to both orthorhombic NiS [24] and the β-NiS phase [25], confirming that a small fraction of Ni participates in the formation of Ni-rich sulfide inclusions.

UV-Vis absorption spectroscopy

Figure 2 displays the UV-Vis absorption spectra of MoS_2 and Ni-doped MoS_2 thin films coated on glass substrates.

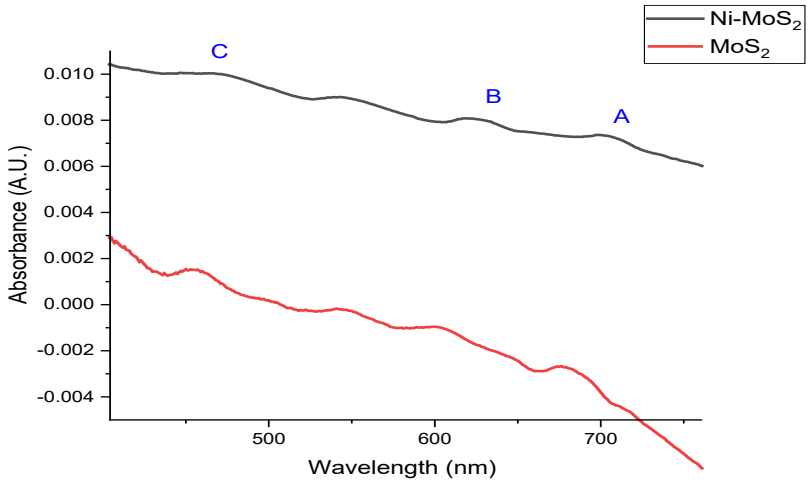

Figure 2: Absorbance spectrum of MoS_2, Ni doped in MoS_2.

Three prominent absorption peaks are observed at approximately 454nm, 610nm, and 678nm. These features are consistent with previously reported data and are assigned to excitonic transitions labeled as C, B, and A, respectively. The A and B transitions, originating from inter-band excitonic transitions at the K points of the Brillouin zone, are characteristic of the 2H polymorph of MoS_2. These absorption bands arise from the energy splitting caused by valence band spin-orbit coupling in 2H-MoS_2 with significant lateral dimensions. Both the A and B absorption bands are intrinsic to the material and are not influenced by surface adsorbates or residual chemicals. The C band, however, is attributed to nearly degenerate multiple excitonic states associated with Van Hove singularities in the electronic density of states of layered MoS_2. Based on this analysis, and in agreement with previous photoluminescence (PL) measurements, it is confirmed that few-layer MoS_2 nanosheets were successfully synthesized.

An additional feature observed at approximately 544nm is likely related to defect states induced by the synthesis process, particularly the relatively high substrate temperature employed. A redshift in the absorption peaks is observed upon Ni doping in MoS_2. Similar spectral shifts have been reported for Ni-doped ZnO and are attributed to sp-d exchange interactions between band electrons and the localized d-electrons of the Ni^{2+} ions, suggesting substitutional doping of Ni^{2+} ions into the host lattice.

Analysis of Ni-doping effects on optical properties

We have conducted a comprehensive study involving the investigation and comparative analysis of the intrinsic band gap of pure samples against nickel-doped samples, specifically examining concentrations of 3%, 5%, and 7%. This analysis was performed utilizing the principles of Tauc's law.

This reduction in band gap energy compared to pristine MoS_2 is a significant outcome of the Ni doping. It suggests that the presence of nickel atoms alters the electronic band structure of the MoS_2. This band gap narrowing can lead to enhanced light absorption in the visible region, potentially improving the material's performance in optoelectronic and photocatalytic applications. The precise mechanism for this band gap reduction in Ni-doped MoS_2 is likely related to the sp-d exchange interactions between the d-electrons of Ni^{2+} ions and the band electrons of MoS_2, as was discussed previously in relation to spectral shifts. Such interactions can lead to the formation of new energy levels within the band gap or a modification of the band edges.

The observed significant reduction in the band gap of MoS_2 upon nickel doping, as detailed previously, points towards a synergistic effect. This effect is understood to arise from the interplay between carbon residues generated during thiourea pyrolysis and the incorporated nickel dopants. Several factors contribute to this phenomenon:

(i) Mid-Gap States: The presence of carbon, along with the nickel dopants, is believed to introduce impurity bands within the band gap. These mid-gap states are likely formed through sp-d exchange interactions occurring between the conduction band electrons and the d-electrons of the Ni^{2+} ions, as supported by existing literature [26].

(ii) Lattice Distortion and Band Tailing: The doping process can induce enhanced lattice distortion. This distortion, in turn, can lead to increased band tailing, effectively broadening the edges of the conduction and valence bands and contributing to a reduced band gap [27,28].

(iii) Formation of Ni-C Interfacial Species: The synthesis conditions may also promote the formation of specific interfacial species involving nickel and carbon. These Ni-C interfacial structures could play a role in modifying the electronic properties [29,30].

(iv) Stabilization of the 1T Phase: Carbon residues can also contribute to the stabilization of the metallic 1T phase of MoS_2. The 1T phase intrinsically possesses different electronic properties compared to the semiconducting 2H phase, often characterized by a smaller band gap or metallic behavior [31].

These combined effects provide a comprehensive explanation for the observed defect-mediated band engineering in these Transition Metal Dichalcogenides (TMDs), aligning with recent research trends in the field [32,33].

Further detailed analysis of the Ni-doped samples reveals a monotonic decrease in the band gap with increasing nickel concentration. Referring to Figure 3, the band gap values are reported to be 1.8, 1.7, 1.68 and 1.59eV for pristine MoS2, %3 Ni, %5 Ni, and %7 Ni, respectively.

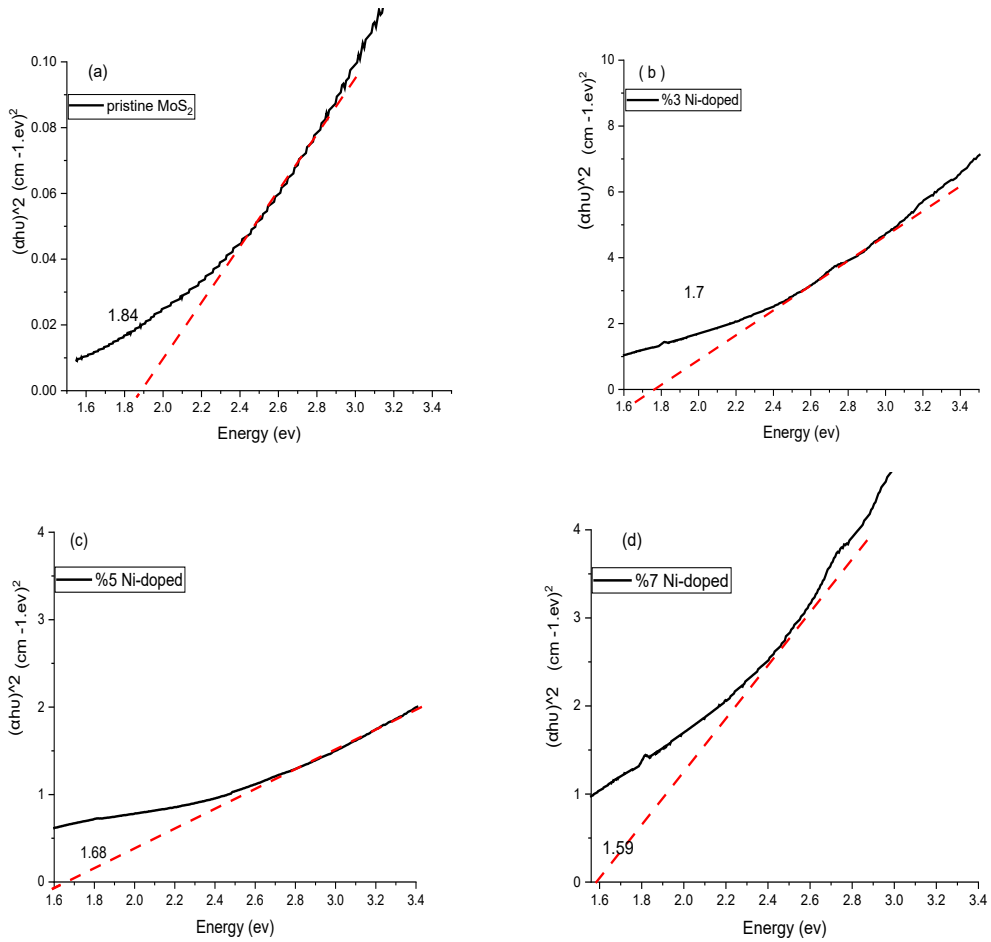

Figure 3: Tauc's plot of pristine MoS_2 and Ni-doped MoS_2, a) pristine MoS_2, b) 3% Ni, c) 5% Ni and d) 7 % Ni doped in MoS_2.

A general narrowing with doping, where the primary mechanism remains the introduction of impurity levels. This narrowing is attributed to substitutional Ni^{2+} ions occupying Mo^{4+} sites, effectively modulating the band gap for potential optoelectronic applications.

Photoluminescence spectroscopy of MoS_2 and Ni-Doped MoS_2

The Photoluminescence (PL) spectra of the synthesized MoS_2 samples provide critical insights into their electronic structure and defectivity. The recombination of electrons and holes within the spin-orbit-split valence bands gives rise to two principal emission peaks, labeled A and B, observed at approximately 680 nm (1.82eV) and 612nm (2.03eV), respectively. The observed low intensity ratio of peak B to peak A (B/A) is indicative of high sample quality and a minimal density of structural defects.

As illustrated in Figure 3, the Gaussian PL peak characteristics of MoS_2 quantum dots (QDs) exhibit a notable dependence on the excitation wavelength. This phenomenon can be attributed to several factors:

(i) potential substrate inhomogeneity arising from non-uniform scattering of constituent QD components;

(ii) the presence of distinct electronic states associated with varied particle aggregation configurations;

(iii) strain induction by higher-energy (shorter wavelength) incident light, which consequentially narrows the energy gap. Given MoS_2's high Young's modulus and exceptional strain tolerance (exceeding 10%), it is recognized as a promising material for strain-engineered applications. Its direct energy gap is known to narrow under minor strains induced by processes such as doping or annealing, and can be further modulated by laser irradiation, a phenomenon also observable in techniques like Raman spectroscopy.

Consistent with the data presented in Figure 4, the photoluminescence (PL) spectra of both undoped and nickel-doped MoS_2 nanosheets exhibit a prominent emission peak within the infrared region. For the undoped sample, this peak is centered at 765nm (1.621eV), whereas for the nickel-doped sample, it is observed at 762nm (1.627eV). This represents a subtle blue shift of approximately 6meV in the Exciton A emission band upon nickel doping, suggesting a modification of excitonic properties. Considering the relatively high excitation energy by laser irradiation (λex=510nm), the observed slight energy gap narrowing in the doped sample might be partially influenced by photo-induced

strain during PL measurements. Furthermore, the reduction in PL intensity in Ni-MoS_2 samples compared to pure MoS_2 indicates significant alterations in the electronic structure and carrier recombination behavior. The higher PL intensity in pure MoS_2 is typically attributed to a greater radiative recombination rate and slower carrier transfer [34]. Conversely, the observed decrease in PL upon doping is directly correlated with enhanced charge transfer efficiency and a reduced electron-hole recombination rate [35]. This suggests that the presence of Ni ions creates new energy levels within the band gap, facilitating faster, non-radiative recombination pathways.

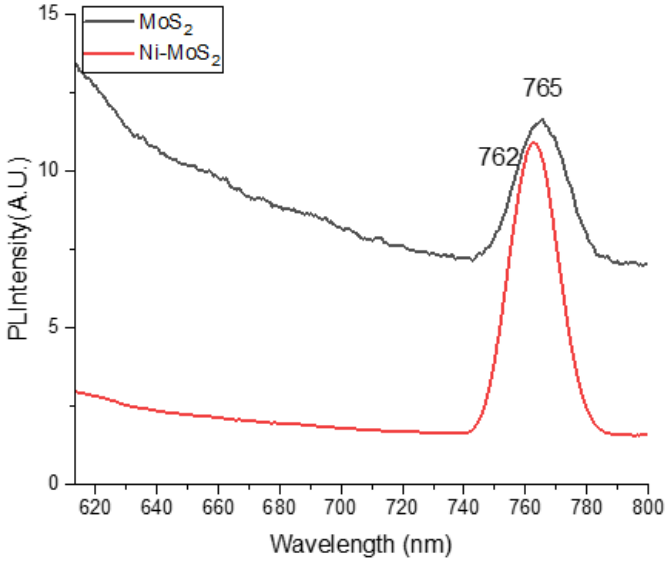

Figure 4: PL spectra of MoS_2 and Ni doped MoS_2 film.

Collectively, the PL data for both undoped and doped MoS_2 structures confirm the formation of few-layer MoS_2 with a direct energy gap of approximately 1.63eV. Nickel doping appears to facilitate exciton formation and potentially enhance the likelihood of monolayer formation through Ni-mediated interlayer interactions. These effects are anticipated to create favorable conditions for improved photocatalytic and magnetic properties in the synthesized materials.

Raman spectroscopic analysis of MoS_2 nanostructures

Raman spectroscopy was employed to confirm the successful synthesis of MoS_2 nanostructures and to elucidate their structural and phase characteristics. The measurements were performed using a 532nm laser excitation source (Takram P50c0R10). The resulting spectrum provides definitive evidence for the presence of the metallic phase (1T or distorted 1T′) of MoS_2 (Figure 5).

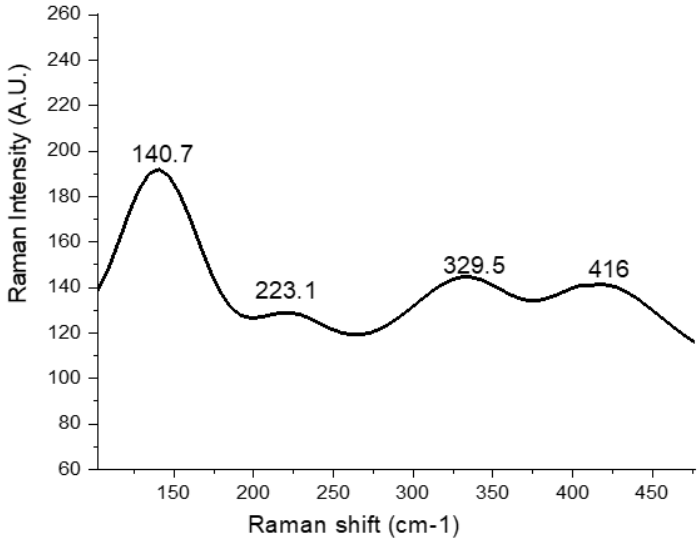

Figure 5: Raman spectroscopy of MoS_2 film.

A prominent peak observed at approximately 140.7cm^{-1} is attributed to the Mo-Mo stretching vibration within the metallic lattice. This is complemented by characteristic peaks at ~223.1cm^{-1} (J_2 mode) and ~329.5cm^{-1} (J_3 mode) [36,37], which are consistent with theoretical predictions of Brillouin zone modifications in octahedrally coordinated metallic MoS_2 [38]. Furthermore, the A_1g phonon mode, observed as a weakened and redshifted feature at ~416cm^{-1}, corroborates the altered electron-phonon interactions characteristic of the metallic polymorph [39,40].

The simultaneous presence of characteristic peaks associated with both the 1T and 2H phases in the Raman spectrum indicates a coexistence of these two structural polymorphs within the sample, which is in excellent agreement with the X-ray Diffraction (XRD) results. The peak at 140.7cm^{-1}, notably absent in the pure 2H phase, is specifically assigned to the vibrational modes of the distorted octahedral structure inherent to the 1T phase.

While the 1T phase is intrinsically less thermally stable than the 2H phase, its observed presence at room temperature can be attributed to kinetic stabilization. This stabilization is likely facilitated by surface interactions with functional groups, such as hydroxyl (OH) moieties or hydrogen atoms, present in the spray pyrolysis synthesis environment. These interactions may contribute to a reduction in the system's free energy, thereby stabilizing the 1T phase.

Structural analysis via X-ray Diffraction (XRD) and FTIR spectroscopy

The vibrational and structural characteristics of the synthesized samples were examined using X-ray Diffraction (XRD) and Fourier-Transform Infrared (FTIR) spectroscopy. XRD patterns exhibit a noticeable shift of the primary (001) diffraction peak toward higher angles (approximately 10°), indicative of a reduction in interlayer spacing. This contraction is typically associated with cation incorporation or structural rearrangements within layered dichalcogenides, in agreement with previous reports [41,42]. Such behavior suggests that nickel ions perturb the MoS_2 lattice, influencing the stacking order and interplanar distances.

FTIR spectroscopy provides complementary evidence regarding chemical bonding and surface functionalities. As displayed in Fig. 7, all samples exhibit a broad absorption band in the 3200-3600cm^{-1} region, corresponding to O-H stretching vibrations. This band reflects the presence of physisorbed moisture, this band reflects the presence of physisorbed moisture, commonly observed in MoS_2 due to surface polarity and residual functional groups potentially originating from precursor preparation or synthesis steps (Figure 6).

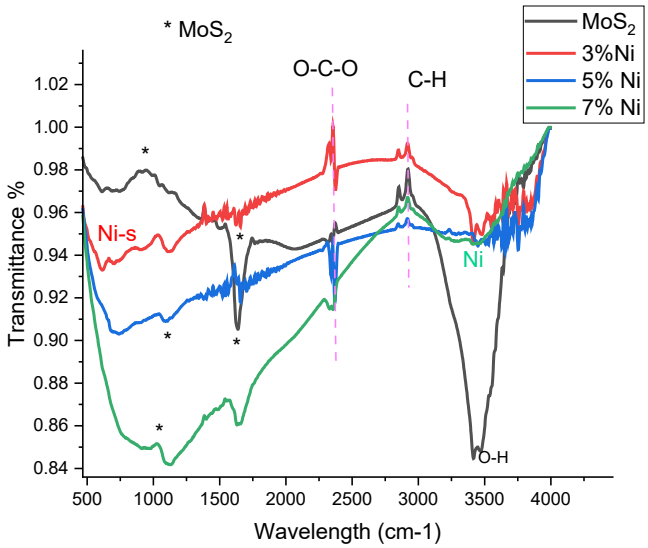

Figure 6: FTIR spectra of MoS_2, % 3 Ni doped MoS_2, % 5 Ni doped MoS_2 and %7 Ni doped MoS_2.

A distinct peak observed around 1000cm^{-1} in all FTIR spectra is attributed to the asymmetric Mo-S stretching vibration, confirming the successful formation of the MoS_2 structure across all synthesized samples [43,44].

Nickel incorporation is evidenced by specific vibrational modes exclusively present in the 3% Ni-doped sample. Peaks at 612cm^{-1} and 926cm^{-1} are assigned to metal-sulfur (Ni-S) and metal-oxygen (Ni-O) bond vibrations, respectively [45]. Notably, the peak at 926cm^{-1} originates from the bending vibrations of Ni-O bonds, indicating their formation due to the incorporation of Ni(II) ions within the MoS_2 lattice. The absence of these Ni-S and Ni-O related peaks in samples doped with higher nickel concentrations (5% and 7%) suggests a fundamental shift in the nickel incorporation mechanism at elevated doping levels.

Weak features around 3450cm^{-1} in all nickel-doped samples are tentatively assigned to the formation of Ni-H bonds during the synthesis process [34], although further investigation may be required for definitive confirmation. A significant observation is the drastic reduction in the intensity of the broad O-H stretching band (~3500-3200cm^{-1}) in Ni-doped samples compared to pristine

MoS_2. This indicates that nickel doping substantially passivates the surface hydrophilicity of MoS_2 by reducing the number of active sites responsible for water adsorption, such as defect sites or oxygen-containing functional groups [46]. This passivation is likely crucial for enhancing photocatalytic or electrocatalytic performance by improving charge carrier dynamics.

Additionally, peaks at 2361cm^{-1} and 2924cm^{-1} correspond to the asymmetric and symmetric O-C-O and C-H stretching vibrations, respectively [47,48]. These may arise from residual organic precursors or atmospheric CO_2 adsorption.

Atomic Force Microscopy (AFM) analysis of MoS_2 and Ni-Doped MoS_2 nanosheets

Atomic Force Microscopy (AFM) was employed to characterize the surface morphology of the synthesized MoS_2 and Ni-doped MoS_2 nanosheets, with representative images presented in Figure 7. The observed surface features, including micro-domes and nanoscale protrusions, are attributed to various phenomena such as mechanical deformation induced by strain or surface oxidation, nucleation effects influenced by synthesis temperature, and stresses within the van der Waals interaction regime of the S-Mo-S layers. These factors, coupled with the inherent elastic properties of MoS_2, lead to swelling in MoS_2 monolayers and the formation of blister-like features, particularly at the MoS_2-substrate interface.

Figure 7 presents typical examples of these domes observed in few-layer MoS_2 and Ni-doped MoS_2. The majority of domes on pristine MoS_2 exhibited radii (R) of approximately 9nm, while Ni-doped MoS_2 samples showed larger average radii, reaching up to 23nm for the Ni-MoS_2 samples. These domes predominantly possessed a round or nearly round base, with larger structures tending towards pyramidal shapes. The formation of these domes is linked to the adsorption of water and impurities via van der Waals forces between the MoS_2 layers and the substrate.

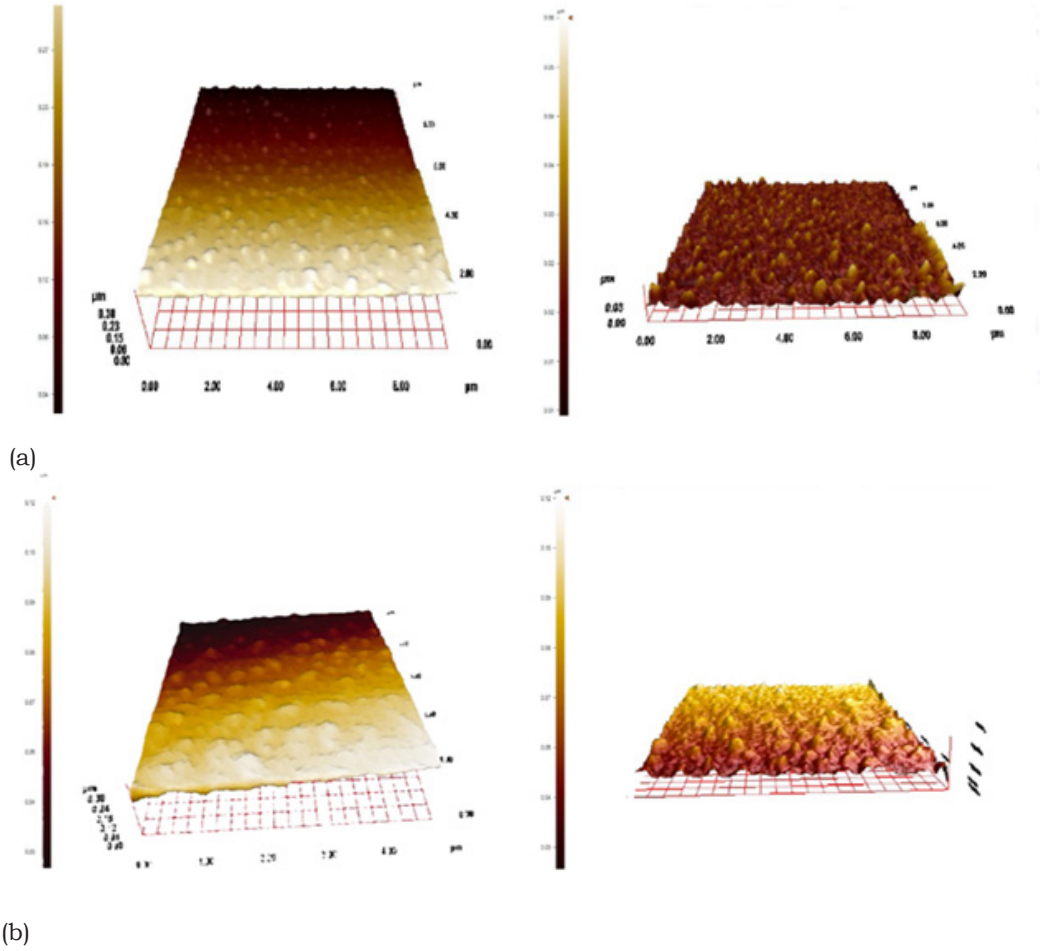

Figure 7: AFM of (a) Ni doped-MoS_2 and (b) MoS_2.

In Figure 7a (Ni-doped MoS_2), the light-colored regions representing domes are notably more extensive compared to the flat, dark regions, and are more prevalent than in pristine MoS_2 (Figure 7b). This increased doming in Ni-doped samples is attributed to the presence of nickel impurities and higher ambient humidity, which facilitates water intercalation between the few-layer MoS_2 and the substrate [49]. Some studies have reported that such bulging, caused by water intercalation, can enhance lubrication at the contact interface [50,51]. Conversely, friction has been shown to increase with rising humidity [52,53].

AFM analysis yielded mean surface roughness (Ra) values of 34nm for pristine MoS_2, 14nm for 3% Ni-doped MoS_2, 21nm for 5% Ni-doped MoS_2, and 29nm for 7% Ni-doped MoS_2. The initial

decrease in surface roughness upon low Ni doping (3%) followed by a progressive increase with higher Ni content (5% and 7%) is likely influenced by factors such as lattice strain arising from the atomic radius mismatch between nickel and molybdenum, and the creation of new nucleation sites during the growth process. The observed non-linear trend of surface roughness with Ni content can be rationalized by a threshold-driven transition from atomically dispersed Ni species to aggregated Ni clusters. Beyond critical loading, cluster growth and coalescence generate pronounced topographic features, which can amplify roughness abruptly rather than gradually. In parallel, Ni-induced local phase transformation (e.g., 2H-to-1T or defect-assisted rearrangements) may alter local bonding configurations and lattice strain, further enhancing roughness in a concentration-dependent manner.

Corroborating the AFM findings, FTIR spectroscopy revealed that pristine MoS_2 exhibited the highest hydroxyl group absorption, which progressively diminished upon nickel incorporation. While moisture absorption in pristine MoS_2 typically elevates friction by increasing interlayer binding energy through hydrogen bonding with sulfur atoms [54], a distinct mechanism governs the tribological behavior of Ni-doped samples. Previous investigations have demonstrated that nickel doping modulates the electronic structure of MoS_2 and generates additional active sites, leading to reduced shear stress and enhanced lubrication performance [55,56]. Consequently, despite its comparatively higher surface roughness among the doped specimens, the 7% Ni-doped MoS_2 demonstrates optimal frictional characteristics, highlighting the beneficial effects of nickel doping on tribological properties.

Photocatalytic activity

The photocatalytic performance of the synthesized pristine MoS_2 and Ni-doped MoS_2 was evaluated by monitoring the degradation of Methylene Blue (MB). The UV-Vis absorption spectra for both the pure MoS_2 and Ni-doped MoS_2 systems are shown in Figure 8. Methylene blue, a hetero-polyaromatic compound containing sulfur and nitrogen atoms, exhibits strong absorbance at 664nm. In the recorded spectra, two distinct absorption peaks are consistently observed around 613nm and 644nm. These peaks are attributed to electronic transitions, including $(n \rightarrow \pi^*)$ transitions involving the unpaired electrons of nitrogen atoms and as the $(\pi \rightarrow \pi^*)$ transitions within the conjugated double bonds of the aromatic ring system. This indicates that an electron excitation transition occurs within the MB solution [57,58]. The percentage of dye degradation was calculated using the following formula:

$$\text{Degradation Efficiency}\,(\%) = \left(1 - \frac{A}{A_0}\right) \times 100 \quad (3)$$

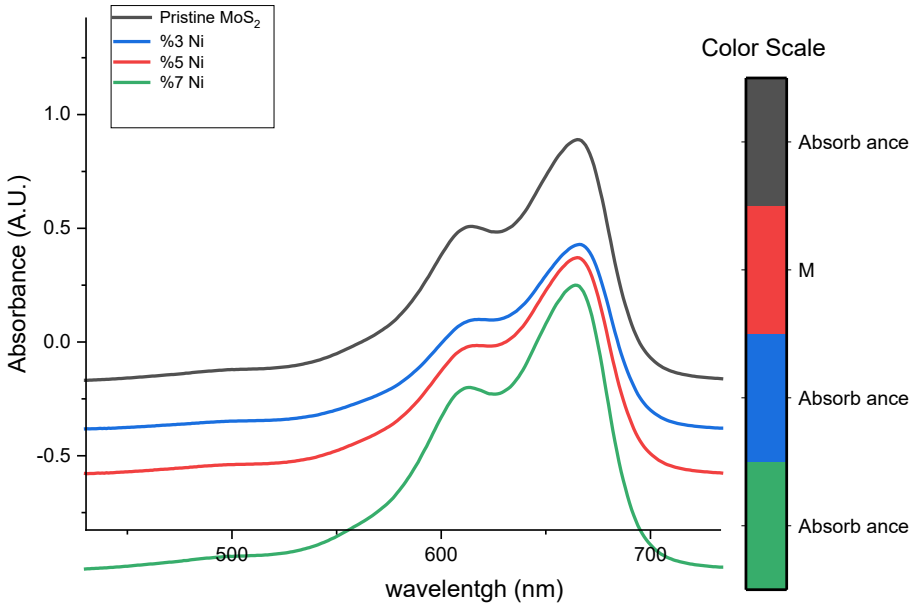

Figure 8: The photocatalytic spectra of pure MoS_2 and Ni-doped MoS_2(3, 5 and 7% Ni) for MB dye.

where A_0 and A are, respectively, the dye solution concentrations before and after photoirradiation for a given time.

Recent studies have reported that the dye degradation efficiency of pristine MoS_2 for MB is relatively low, exhibiting around 19%; however, nanostructured heterojunctions such as $CdS/MoS_2/Bi_2S_3$ have demonstrated extraordinarily high photodegradation efficiencies, reaching 90% [59]. Furthermore, different phases of MoS_2 can enhance degradation efficiency; one study reported methylene blue dye degradation of 72% for 1T-MoS_2 and 98% for 2H-MoS_2, respectively, within 60.0min and 5.0min under visible sunlight [60]. It has also been reported that the MB dye degradation efficiency of pristine MoS_2 increases from 85% to 96% upon doping with 5% Ni into 2H-MoS_2 [61]. This enhancement

is attributed to Ni doping, which is believed to increase the number of uncoordinated atoms at the edge sites of MoS_2, thereby promoting electron transfer across MoS_2 interfaces. Consequently, the photocatalytic activity of MoS_2 is significantly improved [62]. Nickel incorporation into the lattice and the associated defect engineering generates intermediate energy states, thereby tuning the band gap. This enhances the photogenerated electron-hole separation and promotes low-resistance charge-transfer pathways at the interfacial junction, significantly suppressing electron-hole recombination and increasing the electron-transfer efficiency.

Figure 9 illustrates the percentage degradation of methylene blue (MB) over a 120-minute irradiation period as a function of Ni doping concentration in MoS_2. The degradation percentages for MoS_2 doped with 0%, 3%, 5%, and 7% Ni were found to be 53.1%, 81.3%, 96.4%, and 99.4%, respectively.

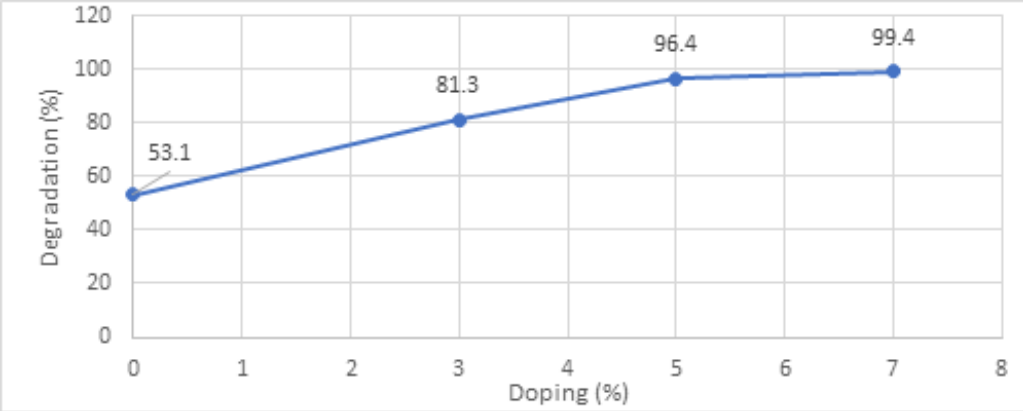

Figure 9: Graphical representations of the effect of Ni-doped MoS_2 on dye degradation of MB.

These results clearly indicate a continuous enhancement in the degradation efficiency of MB dye with an increasing concentration of Ni doping, from 3% to 7%. This observed improvement suggests that doping MoS_2 with Ni plays a crucial role in optimizing its photocatalytic performance.

The enhancement is likely related to the controlled modification of MoS_2 morphology through Ni doping, which potentially increases the number of active sulfur sites available for catalytic reactions [63]. As the number of these active sites increases, the photocatalytic activity of the MoS_2 is significantly enhanced. The maximum degradation efficiency of MB dye was observed with the 7% Ni-doped MoS_2, reaching 99.4%.

Conclusion

This research investigates the synthesis and property engineering of multi-layered MoS_2 thin films using the spray pyrolysis technique on glass substrates, with nickel impurity concentrations varied from 0 to 7 atomic percent. Findings indicate that the presence of oxygen during the synthesis process, by reducing surface energy, impedes the thermodynamic phase transition from the metallic (1T) to the semiconducting (2H) phase, thereby ensuring the coexistence and stabilization of both phases in the final structure. In the evaluation of photocatalytic performance under visible light irradiation, samples containing seven atomic percent nickel demonstrated an enhancement in the degradation efficiency of Methylene Blue (MB) from 53.1% to 99.4%. This significant performance leap is attributed to the synergistic effects stemming from an increased density of structural defects, expanded edge active sites, and improved dynamics of electron-hole pair separation and transfer. This study's findings highlight the efficacy of nickel doping via spray pyrolysis as a strategy for engineering the physicochemical properties of MoS_2, thereby solidifying the high potential of these nanostructures for emerging frontiers in optoelectronics and energy conversion systems.

References

1. Zhao W, Zhang X, Chhowalla M (2021) Layer-dependent optoelectronic properties of MoS_2 and related transition metal dichalcogenides. Advanced Materials 33(15): 2004325.
2. Mu F, Li S, Zhang D, Zhang Q, Hu Z, et al. (2025) Fabricating 2D MoS2 with edge sulfur vacancy defects by heavy ion bombardment shear-exfoliation for enhanced sodium storage. Adv Sci (Weinh) 12(37): e17576.
3. Farooq M, Iqbal T, Khalid NR, Ali A (2022) Simple synthesis of Ni-doped MoS_2 nanoparticles and their application in photocatalytic degradation of organic pollutants. J Sol-Gel Sci Technol 76(20).
4. Reddy BK, Rao SS, Park J (2022) Scalable fabrication of doped MoS_2 thin films via spray pyrolysis for photoelectronic devices. Thin Solid Films 757: 139274.
5. Khan ME, Arshad M, Ahamed MS (2021) Ni-doped MoS_2 nanosheets for improved hydrogen evolution and catalytic activity. Journal of Alloys and Compounds 873: 159839.
6. Zhou L, Lin Y, Wang J (2002) Electronic structure modulation of MoS_2 by Ni doping: A DFT study. Physical Chemistry Chemical Physics 22(19): 10964-10972.
7. Farooq M, Iqbal T, Riaz KN, Mossad A, Abd El-Rehim AF (2022) Simple synthesis of Ni-doped MoS_2 nanoparticles and their application as efficient photocatalyst: experiment and Simulation. Chemical Papers 76: 7493-7506.
8. Katti P, Praveen BM, Devendra BK, Varadaraj S, Kumar JRN (2024) Electrodeposition of Ni-MoS_2 as effective hydrogen evolution reaction catalysts in alkaline media. Hybrid Advances 7: 100296.
9. Soram BS, Dai JY, Thangjam IS, Kim NH, Lee JH (2020) One-step electrodeposited MoS_2 @Ni-mesh electrode for flexible and transparent asymmetric solid-state supercapacitors. J Mater Chem A 24040-2405.

10. Pundi A, Tsai ZT, Chen J, Yu YH, Chang CJ (2024) Enhanced photocatalytic H_2 production activity by loading Ni complex on flower-like MoS_2 nanomaterials. Journal of the Taiwan Institute of Chemical Engineers 161: 105530.

11. Liang T, Hennig RG (2022) Phase stability and electronic properties of 1T and 2H MoS_2 polymorphs under doping and strain. Nano Letters 22(9): 3968-3975.

12. Kumar A, Singh B, Mehta BR (2023) Direct observation of coherent 2H-1T interfaces in mixed-phase MoS_2 nanostructures. ACS Nano 17(4): 3899-3911.

13. Wang Z, Yang H, Zhang J (2021) Mixed-phase MoS_2 heterostructures for advanced photodetectors and field-effect transistors. Advanced Functional Materials 31(42): 2104568.

14. Chen S, Liu G, Zhao Z (2023) Biphasic MoS_2 architectures for efficient photocatalytic and electronic devices. Journal of Materials Chemistry C 11(7): 2285-2296.

15. Hui L, Cheng M, Wang P, Du R, Song L, et al. (2022) Reducing contact resistance and boosting device performance of monolayer MoS2 by in situ Fe doping. Adv Mater 34: 2200885.

16. Zhou J, Zhang X, Xu H (2020) Role of sulfur vacancies in phase transition and catalytic performance of MoS_2. Chemistry of Materials 32(10): 4381-4390.

17. Gong C, Cheng L, Liu Q (2021) Edge-engineering and vacancy control of MoS_2 for high-performance catalysis. ACS Applied Nano Materials 4(6): 5962-5972.

18. Yan Sh, Qiao W, He X, Guo X, Xi L, et al. (2015) Enhancement of magnetism by structural phase transition in MoS_2. Appl Phys Lett106: 012408.

19. Xu W, Yan Sh, Qiao W (2018) Magnetism in monolayer 1T-MoS_2 and 1T-MoS_2H tuned by strain. RSC Adv 8(15): 8435-8441.

20. Kim H, Kim Y Ch, Hwan AY, Yoo Y (2023) In-plane mixed-dimensional 2D/2D/1D MoS_2/$MoTe_2$/Mo_6Te_6 heterostructures for low contact resistance optoelectronics. Chemical Engineering 468: 143678.

21. Gao Y, Wang B, Jiang Z (2023) Uncovering the photoelectronic/catalytic property modulation and applications of 2D MoS2: from the perspective of constructing heterogeneous interfaces. Materials Chemistry A 11 (37): 19736-19763.

22. Ashcroft N, David MN (1976) Solid state physics. Saunders College Publishing.

23. Klug H, Alexander L (1974) X-ray diffraction procedure for polycrystallite and amorphous materials (2nd edn), John Wiley and Sons, New York, USA.

24. Abo-Bakr M, Salman HM, Ismael EM, Ebnalwaled AA (2020) Thiocarbohydrazide as a sulfur source for the preparation of nickel sulfide nanoparticles. 6: 2357-0210.

25. Hayati IN, Mokhlesur RM, Chou SL, Wang JZ, Wexler D, et al. (2011) Rapid synthesis of binary α-NiS-β-NiS by microwave autoclave for rechargeable lithium batteries. Electrochimica Acta 58: 456-462.

26. Mametja S, Mmelesi OK, Mguni LL, Gorimbo J, Liu X (2026) Photo-electrocatalytic water splitting for hydrogen evolution using Ni-based LDH catalysts: Progress and perspectives. Materialstoday 52: 115106.

27. Driss AP, Mesrar M, Elbasset A, Abdi F, Lamcharfi TD, et al. (2025) Tunable optical bandgap and dielectric behavior of $BaTi_{1-x}Fe_xO_3$ ceramics: Insights into structural and optical properties. Resuits in Engineering 27: 106467.

28. Akl AA, Abdel-Rahman M, Aly SA, Abdelmonem D, Salah M (2026) Effective role of Bi doping in controlling the crystallographic, microstructures morphology and optical properties of Cu_2ZnSnS_4 thin films. Next Materials 13.

29. Srivastava AP, Pandey BK (2026) Electronic structure and band-edge engineering of Sc-doped g-C_3N_4: a first-principles study. Discov Chem 3: 234.

30. Bae S, Kim Y, Kim J, Lee J, Kim K, et al. (2017) Ni-C interfacial interactions during pyrolysis of sulfur-containing precursors. Carbon 119: 283-293.

31. Kabir TF, Hossain MI, Rudra S (2025) Phase transformation and electronic structure modulation of 1T-MoS_2 with electronegative non-metal doping as anode material for enhanced potassium-ion battery. Journal of Energy Chemistry 103: 735-748.

32. Hanedar BA, Cengiz OM (2025) Defect dependent electronic properties of two-dimensional transition metal dichalcogenides (2H, 1T, and 1T′ phases). Phys Chem 27: 1809-1818.

33. Hou J, Hyun LCh, Park S, Kim H, Hilal M, et al. (2025) Recent advances in engineering 2D transition metal dichalcogenides for high-performance gas sensing. Sensors and Actuators A: Physical 396: 117195.

34. Batu KB, Shura MW, Dibaba ST (2024) Effect of nickel and selenium co-doping on molybdenum disulfide structure and its electrochemical activity in polysulfide electrolyte. Mater Res Express 11(7): 075901.

35. Farooq M, Iqbal T (2022) Facile hydrothermal synthesis of Cd doped MoS2 nanomaterials for degradation of organic pollutants: correlation between experimental and COMSOL Simulation. J Inorg Organomet Polym Mater 32: 4422-4433.

36. Geng X, Sun W, Wu W, Chen B, Al-Hilo A, et al. (2016) Pure and stable metallic phase molybdenum disulfide nanosheets for hydrogen evolution reaction. Nat Commun 7: 10672.

37. Nayak AP, Pandey T, Voiry D, Liu J, Moran ST, et al. (2014) Pressure-dependent optical and vibrational properties of monolayer molybdenum disulfide. Nano Lett 5036397.

38. Jimenez S, Yang D, Frindt RF, Irwin JC (1991) Raman study and lattice dynamics of single molecular layers of MoS_2. Phys Rev B 44(8): 3955-3962.

39. Sahoo S, Gaur APS, Ahmadi M, Guinel MJF, Katiya RS (2013) Temperature dependent Raman studies and thermal conductivity of few layers MoS_2. Mesoscale and Nanoscale Physics117(17): 9042-9047.

40. Gao B, Zhao Y, Du X, Chen Y, Guan B, et al. (2021) Facile phase transition engineering of MoS_2 for electrochemical hydrogen evolution. J Mater Chem A 9(13): 8394-8400.

41. Guoa Ch, Pana J, Lid H, Lina T, Liud P, et al. (2017) Observation of superconductivity in 1T'-MoS_2 nanosheets. J Mater Chem C 5(41): 10855-10860.

42. Acerce M, Voiry D, Chhowalla M (2015) Metallic 1T phase MoS_2 nanosheets as supercapacitor electrode materials. Nature Nanotechnology 10: 313-318.

43. Feng W, Chen L, Qin M, Zhou X, Zhang Q, et al. (2015) Flower-like PEGylated MoS_2 nanoflakes for near-infrared photothermal cancer therapy. Scientific Reports 5: 17422.

44. Liu T, Wang C, Gu X, Gong H, Cheng L, et al. (2014) Drug delivery with PEGylated MoS_2 nano-sheets for combined photothermal and chemotherapy of cancer. Adv Mater 26: 3433-3440.

45. Alhassan S, Alshammari AH, Alotibi S, Alshammari Kh, Mohamed WS, et al. (2024) Structural and optical properties of nickel-doped zinc sulfide. Nano Materials 14: 1599.

46. Hao M, Li C, Wu M, Li Q, Xiao Z, et al. (2024) Superhydrophilicity and superaerophobicity Ni/Ni_3S_4/1T-MoS_2 for hydrazine-assisted seawater splitting. Journal of Colloid and Interface Science 679: 966-974.

47. Infrared and Raman Characteristic Group Frequencies: Tables and Charts Wiley, (3rd edn).

48. Suthar P, Patidar D (2024) Hydrothermally synthesized MoS_2 NFs toward efficient supercapacitor and fast photocatalytic degradation of MB. Research on Chemical Intermediates 50: 3569-3595.

49. Xua C, Yeb Z, Egberts P (2023) Intercalated water-induced hysteretic friction behavior of graphene, h-BN, and MoS_2. Applied Surface Science 603: 157442.

50. Gong P, Ye Z, Yuan L, Egberts P (2018) Evaluation of wetting transparency and surface energy of pristine and aged graphene through nanoscale friction. Carbon 132: 749-759.

51. Dou X, Koltonow AR, He X, Jang HD, Wang Q, et al. (2016) Self-dispersed crumpled graphene balls in oil for friction and wear reduction. Proceedings of the National Academy of Sciences 113(6): 1528-1533.

52. Arif T, Colas G, Filleter T (2018) Effect of humidity and water intercalation on the tribological behavior of graphene and graphene oxide. ACS Applied Materials and Interfaces 10(26): 22537-22544.

53. Xu K, Cao P, Heath JR (2010) Graphene visualizes the first water adlayers on mica at ambient conditions. Science 329: 1188-1191.

54. Yang Z, Bhowmick S, Sen FG, Alpas AT (2021) Microscopic and atomistic mechanisms of sliding friction of MoS_2: Effects of undissociated and dissociated H_2O. Applied Surface Science 563: 150270.

55. Prakash K, Harish S, Kamala KS, Logu T, Shimomura M, et al. (2023) Perspective on ultrathin layered Ni-doped MoS_2 hybrid nanostructures for the enhancement of electrochemical properties in supercapacitors. Journal of Energy Chemistry 80: 335-349.

56. Karkee R, Guerrero E, Strubbe DA (2021) Structural studies of Ni-doped MoS_2 monolayers and polytypes using density functional theory. Bulletin of the American Physical Society 66(1).

57. Hidayat R, Wahyuningsih S, Fadillah G, Ramelan AH (2022) Highly visible light photodegradation of RhB as synthetic organic dye pollutant over TiO_2-modified reduced graphen oxide. Journal of Inorganic and Organometallic Polymers and Materials 32: 85-93.

58. Liu ST, Huang J, Ye Y, Zhang AB, Pan L, et al. (2013) Microwave enhanced Fenton process for the removal of methylene blue from aqueous solution. Chemical Engineering Journal 215: 586-590.

59. Nazir A, Tahir MS, Kamal GM, Zhang X, Tahir MB, et al. (2023) Fabrication of ternary MoS_2/CdS/Bi_2S_3-based nano composites for photocatalytic dye degradation. Molecules 28(7): 3167.

60. Jadha J, Waghadkar Y, Padwal Y, Hashem M, Kekade S, et al. (2025) Enhanced dye degradation using 2H-MoS_2 and 1T@2H-MoS_2: A comparative study. Journal of Solid-State Electrochemistry 29: 3217-3228.

61. Khan MI, Hasan MS, Bhatti KA, Hina R, Wahab A, et al. (2020) Effect of Ni doping on the structural, optical and photocatalytic activity of MoS_2, prepared by Hydrothermal method. Mater Res Express 7: 015061.

62. Xiaoyan M, Jinquan L, Changhua A, Juan F, Yuhua C, et al. (2016) Ultrathin Co (Ni)-doped MoS_2 nanosheets as catalytic promoters enabling efficient solar hydrogen production. Nano Research 9: 2284-2293.

63. Kumar P, Song MI, Hong S, Kim EH, Gopannagari M, et al. (2017) Optimization of active sites of MoS_2 nanosheets using nonmetal doping and exfoliation into few layers on CdS nanorods for enhanced photocatalytic hydrogen production. ACS Sustainable Chemistry & Engineering 5: 7651-7658.